MATERIALS CHEMISTRY
FRONTIERS

RESEARCH ARTICLE

View Article Online
View Journal | View Issue

Cite this: *Mater. Chem. Front.*, 2018, **2**, 1554

AIE-based super-resolution imaging probes for β-amyloid plaques in mouse brains†

Ya-Long Wang,‡[a] Cheng Fan,‡[a] Bo Xin,‡[ab] Jian-Ping Zhang,[ab] Ting Luo,[ab] Ze-Qiang Chen,[a] Qi-Yuan Zhou,[a] Qi Yu,[a] Xiang-Ning Li,[ab] Zhen-Li Huang,[ab] Chong Li,*[a] Ming-Qiang Zhu*[a] and Ben Zhong Tang*[c]

Fluorescence microscopy is an intuitive detection method of β-amyloid (Aβ) fibrillation, which usually occurs in early-stage Alzheimer's disease. With the aid of single-molecular localization of reversibly-activated fluorogens, the limit of optical diffraction in fluorescence microscopy can be overcome and the imaging resolution can be promoted to the sub-100 nm boundary. Aggregation-induced emission (AIE) is the fluorogenic emission behavior in which fluorescence is significantly enhanced due to the restriction of intramolecular motion when the fluorogens aggregate together or bind with specific targets. Reversible binding events of AIE-active fluorogens cause fluorescence switching enabling single-molecular localization and super-resolution imaging. Here, we report a series of super-resolution fluorescent probes with AIE activity, which are used for the detection and super-resolution imaging of fibrillar amyloids. The AIE-active fluorogens show superior *in vitro* sensitivity to fibrillar amyloids of hen egg white lysozyme (HEWL), which is usually used as a model protein for amyloid studies, with the limit of detection down to 63.71 nM. The fluorescence colocalization imaging indicates the excellent *ex vivo* targeting capability of Aβ plaques in mouse brain slices, with the colocalization degrees more than 90%. Based on the reversible binding between AIE-fluorogens and Aβ fibrils, the AIE-based super-resolution imaging of *in vitro* Aβ fibrillation in tubes and *ex vivo* Aβ plaques in mouse brain slices is accomplished. The detailed structure information reveals that Aβ plaques in the mouse brain are composed of numerous radiant nanofibrils with an optical imaging resolution of about 30 nm.

Received 4th May 2018,
Accepted 13th June 2018

DOI: 10.1039/c8qm00209f

rsc.li/frontiers-materials

Introduction

Alzheimer's disease (AD) is a clinically common degenerative lesion of the central nervous system, which could result in memory disorders, aphasia, apraxia, agnosia, visuospatial skills and executive dysfunctions.[1,2] So far, research has shown that the formation of senile plaques due to the abnormal deposition of β-amyloid (Aβ) is the main pathological feature of AD.[2–4] There is no apparent sign at the early stage of AD until severe symptoms occurs irretrievably. Hence, the early detection of Aβ deposits and the detailed structural characterization of amyloid plaques play an important role in the early detection and treatment of AD.[5] Fluorescence microscopy has been widely applied in biomedical applications, in view of the advantages of high sensitivity, high contrast, high resolution, intuitive imaging and fast imaging speed.[6–9] However, the spatial resolution of fluorescence microscopy is limited to approximately 200 nm in the imaging plane imposed by light diffraction. Recently, the diffraction limitation has been overcome by super-resolution techniques of fluorescence imaging, which have better spatial and temporal resolution.[10–15] Fluorescence microscopy integrated with super-resolution imaging could intuitively observe Aβ deposits with even higher resolution to enable clear morphological investigation of Aβ plaques in mouse brain slices.

In 2001, the concept of aggregation-induced emission (AIE) was introduced, which is opposite to aggregation-caused quenching (ACQ) suffered by traditional fluorescent materials due to the intense intermolecular π–π stacking interactions.[16] AIE fluorogens have been widely applied in biological fields owing to the higher fluorescence intensity of AIE fluorogens in the aggregated state.[6,17–22] Compared with traditional organic dyes, AIE-involved imaging systems show better features, such

[a] *Wuhan National Laboratory for Optoelectronics, College of Optical and Electronic Information, Huazhong University of Science and Technology, Wuhan, Hubei 430074, China. E-mail: mqzhu@hust.edu.cn, chongli@hust.edu.cn*
[b] *Department of Biomedical Engineering, Key Laboratory for Biomedical Photonics of Ministry of Education, Huazhong University of Science and Technology, Wuhan, Hubei 430074, China*
[c] *Department of Chemistry, The Hong Kong University of Science & Technology, Clear Water Bay, Kowloon, Hong Kong, China. E-mail: tangbenz@ust.hk*

† Electronic supplementary information (ESI) available. See DOI: 10.1039/c8qm00209f

‡ These authors contributed equally to this work (Y.-L. Wang, C. Fan and B. Xin).

as large absorptivity, high luminosity, reversible emission due to the binding/dissolution equilibrium[23] and good anti-photobleaching performance.[6] Another noteworthy advantage of AIE-based fluorescent imaging is that the washing step may often be unnecessary because AIE-active fluorogens emit only upon binding with targets, which is preferred in bioimaging applications. Hence, if Aβ binding groups are introduced into AIE molecules, strong fluorescence could be detected upon staining because of the aggregating of AIE molecules in the lesions of the brain section. A systematic investigation on the specific binding of fluorescent probes for Aβ deposits is in urgent demand although there are several reports that fluorescent probes have been used for the detection of Aβ deposits.[4,5,24–27] It is noteworthy that AIEgen has been used to detect a similar protein fibrillation to Aβ deposits.[28–30] AIE-active probes seem ideal for the detection of Aβ deposits because their emission is associated with aggregating or binding events. Water-miscible AIE molecules may act as excellent amyloidal probes because of their negligible emission in aqueous buffer and minimal interference from the background. Additionally, aromatics in AIE-active molecules may facilitate molecular docking in the hydrophobic domains of Aβ fibrils, hence activating the restriction of intramolecular motion (RIM) process and switching on emission. Therefore, AIE-active probes for the detection of Aβ deposits are expected to flourish. However, to obtain detailed information of Aβ plaques with nanoscale resolution, AIE-based super-resolution imaging of Aβ deposits in brain tissue is desirable. There are several reports on the super-resolution imaging of Aβ fibrils *in vitro*.[31–35] But super-resolution imaging based on the AIE concept and the mechanism of Aβ plaques is not yet reported.

Considering the strong demand of super-resolution imaging agents specific to Aβ deposits, here, we design and synthesize a series of AIE-active molecules with nearly planar donor–acceptor structures, which facilitate molecular insertion into the binding site, causing RIM and thus enhanced fluorescence (Fig. 1). The probes emit negligible fluorescence in solution, while in the aggregated state, they emit strong fluorescence due to RIM.[6] Piperidine and dimethylamino-substituted groups are introduced into the molecular structures as electron donating and also binding groups for Aβ. DM-BZ, PD-BZ and PD-NA were synthesized by a typical nucleophilic addition reaction of aldehydes and 2-(4-bromophenyl) acetonitrile with high yields of 75–85% (Scheme S1, ESI†). PD-NA-TEG was synthesized by Suzuki reaction.

Results and discussion

The maximum UV-Vis absorption peaks of DM-BZ, PD-BZ, PD-NA and PD-NA-TEG in THF are located at 390 nm, 380 nm, 405 nm and 397 nm, respectively (Fig. S1, ESI†). The fluorescence of DM-BZ, PD-BZ, PD-NA and PD-NA-TEG in THF is negligible but their solid-state films emit strong fluorescence from green to yellow with the peak wavelength of 500–546 nm (Table S1, ESI†). Since the photoluminescence quantum yield (PLQY) of PD-BZ is slightly higher than that of DM-BZ, piperidine is selected as the modified electron-donating group while the benzene ring was replaced by a naphthalene ring, which has better rigidity and conjugation. As expected, the PLQYs of PD-NA and PD-NA-TEG in the aggregate state increase to 7.88% and 9.10%, respectively (Table S1, ESI†). The four fluorogens exhibit AIE features due to the RIM mechanism.[6] For DM-BZ

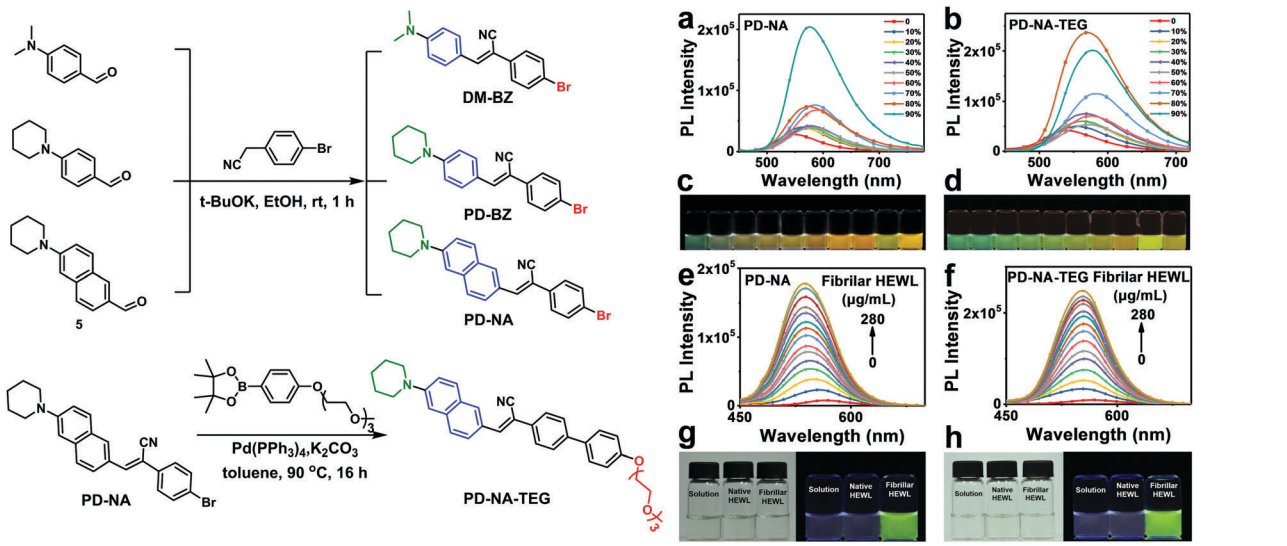

Fig. 1 Schematic synthesis and optical properties of AIE. Synthesis route and structure of DM-BZ, PD-BZ, PD-NA and PD-NA-TEG (left). Emission spectra of (a) PD-NA and (b) PD-NA-TEG in THF-water with different water contents, (the excitation wavelength is 405 nm). The concentration of dyes is kept at 1.0×10^{-5} M. Fluorescence spectra of (c) PD-NA and (d) PD-NA-TEG in THF-water with different water contents under 365 nm irradiation. Emission spectra of (e) PD-NA and (f) PD-NA-TEG in 30% EtOH/H_2O with different fibrillar HEWL contents (the excitation wavelength is 405 nm). The concentration of the dyes is kept at 3 μM. Photos of (g) PD-NA and (h) PD-NA-TEG in 30% EtOH/H_2O, with native HEWL (280 μg mL^{-1}) and fibrillar HEWL (280 μg mL^{-1}) under room light (left) and 365 nm irradiation (right).

and PD-BZ, the PL intensity shows no obvious change when the water faction increased from 10% to 80%. However, the PL intensity is significantly enhanced as the water faction increased from 80% to 90% (Fig. S2, ESI†). Both DM-BZ and PD-BZ exhibit a weak blue-green emission in 90% water/THF nanoaggregates, which match with the PLQY measured in the aggregated state (Table S1, ESI†). For PD-NA and PD-NA-TEG, the PL intensity increases gradually with the water faction from 0 to 90% (Fig. 1a–d). The maximum PL emission was measured when the water faction is increased to 90% and 80% for PD-NA and PD-NA-TEG, respectively. For PD-NA-TEG, the emission peak at 90% water content is a little lower than that at 80% water content with a slight red shift, indicating that the packing modes of the luminogen molecules may change due to aggregating into larger particles and precipitating quickly, which could influence the fluorescence color and intensity.[36–40] The emission shows a red-shift trend due to the intermolecular charge transfer effect of the dyes with D–A structure.[41]

Hen egg white lysozyme (HEWL) is often selected as a model protein for amyloid studies due to its ability to easily form amyloid aggregates. We have compared the detection performance of PD-NA and PD-NA-TEG for amyloid fibrils of HEWL. PD-NA and PD-NA-TEG dissolve well in water containing 30 v/v% ethanol and show weak fluorescence due to non-radiative transitions produced by free intramolecular motion. PD-NA and PD-NA-TEG in water containing 30 v/v% ethanol remain non-emissive no matter whether before or after the addition of native HEWL in phosphate-buffered saline (PBS). Their fluorescence is switched on when a small amount of fibrillar HEWL is added (Fig. 1e and f). They remain weakly fluorescent in native HEWL solution but become emissive in the presence of amyloid fibrils of HEWL (Fig. 1g and h). The probe solutions in the presence of both native and fibrillar forms of HEWL are transparent under room light. The mixture of probes and fibrillar HEWL emits a strong green light while that of the probes and native HEWL shows almost no fluorescence. Similar results are observed for DM-BZ and PD-BZ (Fig. S3, ESI†). All four fluorogens can discriminate between the native and fibrillar forms of HEWL and work efficiently for quantitative analysis of amyloidal fibril formation (Fig. S3e, ESI†). The limits of detection of DM-BZ, PD-BZ, PD-NA and PD-NA-TEG for HEWL fibrils ware calculated to be 152.86 nM, 87.64 nM, 160.70 nM and 63.71 nM, respectively (Table S2, ESI†). PD-NA-TEG shows better detection capability than the other three AIE fluorogens, which is probably mainly due to the introduction of a TEG hydrophilic chain.

Since AIE-active fluorogens show specific sensitivity to HEWL amyloid fibrillation and dynamic binding capability to HEWL fibrils, we launch translational research for the AIE-based super-resolution imaging of HEWL amyloid fibrils. We first investigated the *in vitro* fluorescence and super-resolution imaging of fibrillar HEWL samples utilizing PD-NA-TEG (Fig. 2) as staining agents. Well-defined fibril-like HEWL aggregates are observed in the SEM image (Fig. 2a) while only vague shapes appear in the fluorescence microscope (Fig. 2b) and bright field images (Fig. 2d). The detailed nanostructures of the HEWL aggregates are obtained (Fig. 2c) with the high photon count distribution of each event above 1000 (Fig. 2e). The full-width at half maximum of the localized single fluorescence point was determined from Gaussian deconvolution to be as low as 28 nm (Fig. 2f). The overall resolution of a diffraction-unlimited image determined by Fourier ring correlation (FRC) is found to be 38.13 ± 2.27 nm (Fig. 2g). The super-resolution imaging of HEWL amyloid fibrils provides much advantage over SEM and TEM in the sample processing of organic materials and biological tissues due to their insulation and the ease of fluorescence labelling.

To evaluate the *ex vivo* affinity of these AIE probes for Aβ plaques in the lesion tissue of mouse brains, neuropathological fluorescence staining of Aβ plaques in the brain was carried out

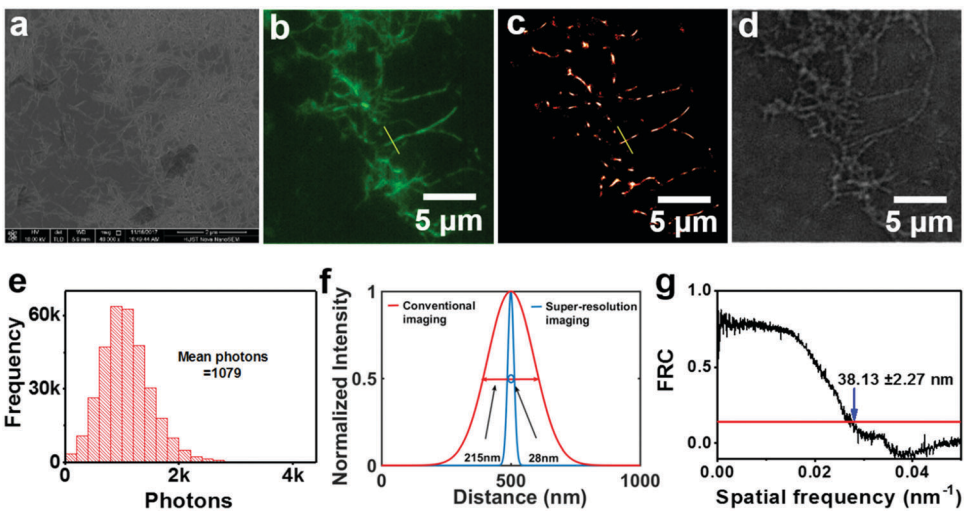

Fig. 2 Super-resolution imaging of fibrillar HEWL for PD-NA-TEG. (a) SEM image of fibrillar HEWL. (b) Conventional fluorescence image. (c) Super-resolution image corresponding to the same field of the fluorescence image. (d) Bright field image. (e) The photon count distribution for each event. (f) Conventional fluorescence and super-resolution imaging cross-sectional profiles. (g) Fourier ring correlation (FRC) of the localizations in (c) (the excitation wavelength is 405 nm).

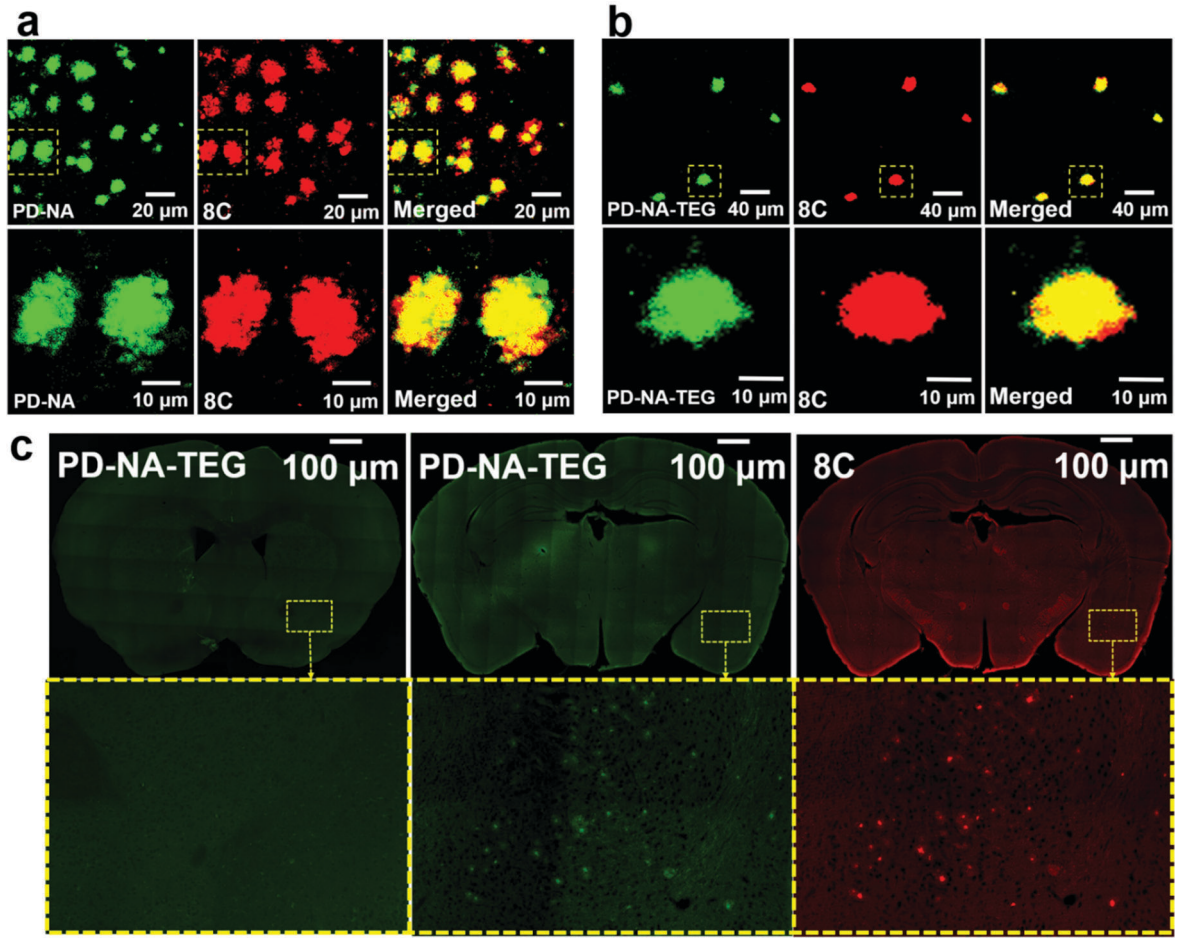

Fig. 3 Fluorescence colocalization imaging of Aβ deposits in the brain slices of a Tg mouse (Tg6799, 9-month old, male) for PD-NA and PD-NA-TEG with 8C. (a) Confocal images of the brain slices of a Tg mouse (Tg6799, 9-month old, male) stained with PD-NA and 8C. PD-NA (left), 8C (middle) and overlay (right). (b) Confocal images of the brain slices of a Tg mouse (Tg6799, 9-month old, male) stained with PD-NA-TEG and 8C. PD-NA-TEG (left), 8C (middle) and overlay (right). (c) Fluorescence images of the whole brain slices of a wild-type control mouse (SOM:cre;Ai14, 12-month old, male) for PD-NA-TEG (left) and a Tg mouse (Tg6799, 9-month old, male) for PD-NA-TEG (middle) and 8C (right). The bottom panels of (a), (b) and (c) are partially enlarged images of the yellow square area, respectively.

using brain tissue sections of a transgenic (Tg) mouse (Tg6799, 9-month old, male). The Tg mouse (Tg6799, 9-month old, male), which is specifically engineered to overproduce Aβ plaques in the brain, has been extensively used to evaluate the specific binding of Aβ deposits in *ex vivo* and *in vivo* experiments. A reported fluorescent probe 8C with verified affinity for the binding of Aβ deposits was selected as the dye for fluorescence colocalization.[5] The fluorescence colocalization images indicate that many fluorescent spots of about 20 μm are observed in the brain sections stained by DM-BZ, PD-BZ, PD-NA, PD-NA-TEG and 8C (Fig. S4, ESI† and Fig. 3). The merged images indicate that the green spots of PD-NA (Fig. 3a) and PD-NA-TEG (Fig. 3b) show almost complete coincidence with the red spots of 8C. The two images overlap well with the Manders' overlap coefficient (R) of 0.91, 0.92, 0.92 and 0.94 for DM-BZ, PD-BZ, PD-NA and PD-NA-TEG with 8C, respectively. The Pearson's correlation coefficient (PCC) was calculated to be 0.61, 0.62, 0.70 and 0.72 for DM-BZ, PD-BZ, PD-NA and PD-NA-TEG with 8C, respectively, by ImageJ colocalization analysis, indicating a good correlation. The fluorescence colocalization data indicate that the four AIE compounds are excellent probes, especially PD-NA and PD-NA-TEG, for binding with Aβ plaques in the mouse brain. In addition, the brain-wide fluorescence imaging indicates that Aβ plaques are observed in the whole brain slice of a Tg mouse staining with PD-NA-TEG and 8C while no obvious Aβ spots are detected in the wild-type mouse whole brain slices (Fig. 3c). We investigated and compared the *ex vivo* fluorescence and super-resolution imaging of Aβ plaques in the brain slices of a Tg mouse in an identical selected area, utilizing DM-BZ, PD-BZ, PD-NA and PD-NA-TEG as staining agents (Fig. S5, ESI† and Fig. 4). It seems there is no significant difference between the normal tissue and the lesion regions in the bright field image (Fig. 4a and g). However, the conventional fluorescence imaging reveals the emergence of Aβ deposits (Fig. 4b, h, Fig. S5b and f, ESI†). However, the specific topographical features are inaccessible from the conventional fluorescence imaging. In the super-resolution imaging mode, the morphology of Aβ plaques in the brain slices is optically resolved (Fig. 4c, i and Fig. S5c and g, ESI†). The most significant discovery is that each Aβ plaque is

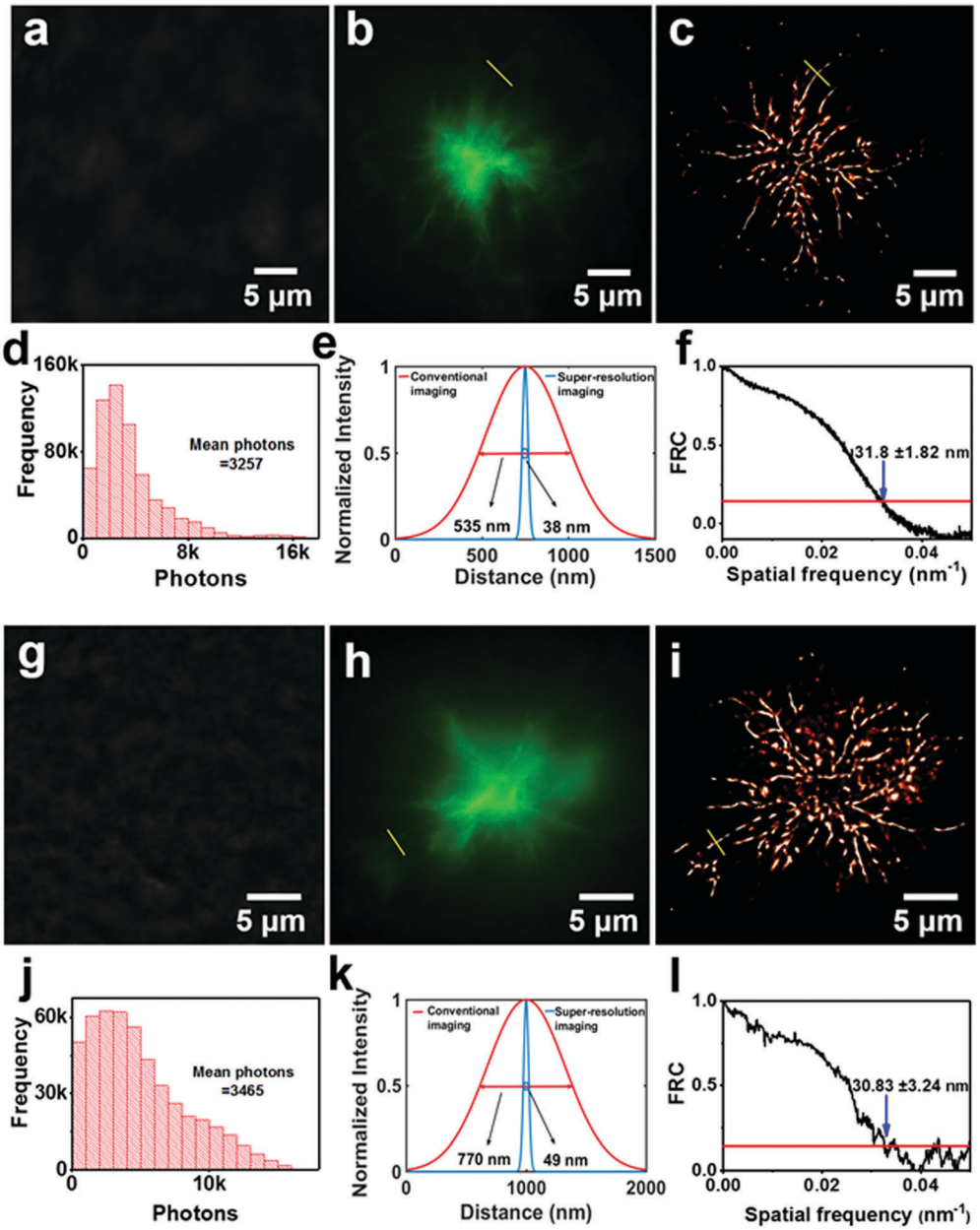

Fig. 4 Super-resolution imaging of Aβ deposits in the brain slices of a Tg mouse (Tg6799, 9-month old, male) for PD-NA (top) and PD-NA-TEG (bottom). (a and g) Bright field images. (b and h) Conventional fluorescence images. (c and i) Super-resolution images corresponding to the same field as the fluorescence images. (d and j) Photon count distribution for each event. (e and k) Conventional fluorescence and super-resolution imaging cross-sectional profiles of PD-NA and PD-NA-TEG. (f and l) Fourier ring correlation (FRC) of the localizations in (c) and (i) (the excitation wavelength is 405 nm).

composed of a lot of radiant nanofibers grown from the centre, which probably means that the Aβ deposit is initiated somewhat by the nucleation due to protein β-sheet transition. The mean photon numbers of DM-BZ and PD-BZ are counted to be 1857 and 1530, while those of PD-NA and PD-NA-TEG are 3257 and 3465, indicating the excellent imaging activity of PD-NA (Fig. 4d) and PD-NA-TEG (Fig. 4j). The full width at half maximum of a single emitting spot of PD-NA and PD-NA-TEG is determined to be 38 nm (Fig. 4e) and 49 nm (Fig. 4k), respectively. The overall resolution of a diffraction-unlimited image determined by Fourier ring correlation (FRC) is found to 31.80 ± 1.82 nm and 30.83 ± 3.24 nm of PD-NA (Fig. 4f) and PD-NA-TEG (Fig. 4l), respectively, indicating that PD-NA and PD-NA-TEG possess excellent super-resolution performance targeting to Aβ plaques in the mouse brain.

AIE-active fluorogens have a unique advantage in the detection of Aβ plaques due to the higher fluorescence intensity of AIE-active fluorogens in the aggregate state than that in solution. Hence, strong fluorescence could be detected if AIE-active fluorogens bind specifically to the site of the lesion in the brain slices of a Tg mouse. Here, AIE-active fluorogens are used for the *in vitro* detection of HEWL amyloid fibrillation. The results show that the AIE-active fluorogen probe could be specifically sensitive to

fibrillar HEWL, but not native HEWL at lower concentrations (<200 μg mL^{-1}). The second investigation is the colocalization of AIE-active fluorogens and reported dye 8C for Aβ plaques in the brain slices of a Tg mouse. The results indicate that the dyes, especially PD-NA and PD-NA-TEG, have excellent specific-binding capacity for Aβ plaques in the brain slice. However, it seems that the specific morphology in detail of Aβ plaques could not be observed using the traditional fluorescence imaging. To obtain detailed information of Aβ plaques with nanoscale resolution, the super-resolution imaging of Aβ plaques in the brain slices of a Tg mouse is put into practice through the reversible fluorescence on/off switching of AIE-active fluorogens, resulting in dynamic binding specific to Aβ plaques. Here, the AIE phenomenon plays a key role in forming the fast photoswitching behavior on Aβ plaques. The AIE molecules emit fluorescence when binding to Aβ plaques. Also, the binding AIE molecules are dissolved again into the solvent in a stochastic style, causing the AIE on the binding point to disappear. Originating from the dynamic balance of the binding/dissolving processes, the fluorescence stochastic on/off switching on the target structure satisfies the requirement of super-resolution imaging based on single molecule localization. A clearer morphology of Aβ plaques in mouse brain slices is observed showing that the Aβ plaques are composed of a lot of radiant nanofibers stemming from the center, which probably means that Aβ deposition is initiated somewhat by nucleation due to protein β-sheet transition. The accessibility to such detailed information could be of significance to address the growth mechanism of amyloids and to develop new diagnostic agents and therapeutic drugs for the detection and treatment of Alzheimer's diseases associated with the conformational disorders of proteins. In the future, water-soluble AIE-active probes for the detection and super-resolution imaging of Aβ-positive plaques are expected to thrive.

Conclusions

In conclusion, four AIE-active fluorescent probes are synthesized and used for the detection of Aβ fibrils and super-resolution imaging of Aβ deposits in the brain slices of a Tg mouse (Tg6799, 9-month old, male). As the fluorescence turn-on imaging is based on the novel AIE concept, the experiments showed that AIE-active fluorogens are excellent fluorescent probes for the binding of Aβ plaques in mouse brains. Further in-depth studies suggest that the AIE-active probes can be used for the super-resolution imaging of Aβ plaques in mouse brains. PD-NA and PD-NA-TEG are both excellent super-resolution imaging agents of Aβ plaques with the mean photon number more than 3000 with Gaussian distribution. From the super-resolution images, the morphology of the Aβ plaques in the brain slices is extraordinarily clear, showing that they are composed of many radiant nanofibrils, affording detailed information of Aβ fibrillation with about 30 nm of optical resolution. The accessibility to such detailed information could be ultimately used to address the growth mechanism of amyloids and to develop new diagnostic agents and therapeutic drugs for the detection and treatment of Alzheimer's diseases associated with conformational disorder of proteins.

Experimental

Materials and instrumentation

All commercially available starting materials, reagents and solvents were used as supplied, unless otherwise stated, and were purchased from Aladdin, Energy, and Sinopharm Chemical Reagent Co. Ltd. All reactions were carried out under a dry nitrogen atmosphere and the temperatures were measured externally. THF and toluene were dried using sodium wire and benzophenone as the indicator. All experiments were performed on a 400 MHz Bruker AV400 or AV600 spectrometer at room temperature using $CDCl_3$ or DMSO-d_6 as the solvent. UV-Vis absorption and photoluminescence emission spectra of the compounds were recorded on a Shimadzu UV-VIS-NIR Spectrophotometer (UV-3600) and Edinburgh instruments (FLS 920 spectrometers), respectively. Fluorescence observation was performed using a confocal laser-scanning microscope (Zeiss LSM710, Germany). The microscope is based on a commercial microscope stand (Olympus IX73P2F) and imaging was carried out using a 100 × 1.49 NA oil-immersion TIRF objective (UAPON 100XOTIRF, Olympus). Two solid-state lasers including a 405 nm solid-state laser (OBIS 405 LX, Coherent, 50 mW) and a 561 nm solid-state laser (OBIS 561 LS, Coherent, 150 mW) were used. A dichroic mirror (DM: ZT561rdc-xr, Chroma) and a single band filter (EM: ET630/75 m, Chroma) were used to separate the collected fluorescence from the scattering laser and impurity fluorescence.

Preparation of HEWL amyloid fibrils

Lyophilized HEWL (Sigma-Aldrich) was dissolved at 10 mg mL^{-1} (700 μM) in a 10 mM, pH 3 sodium acetate–acetic acid buffer solution with 0.1 M NaCl. The solution was incubated in a 70 °C oil bath and magnetically stirred at 250 rpm for 12 h. The initially clear solution was observed to form cloudy aggregates after 1 h of incubation. The samples were stored at 4 °C and observed to undergo no noticeable degradation over the course of 1 month.

In vitro fluorescence staining of Aβ plaques in transgenic mouse brain sections

Paraffin-embedded brain tissue from transgenic mice (Tg6799, 9-month old, male) was used for *in vitro* fluorescence staining. The brain sections were deparaffinized with 2 × 20 min washes in xylene, 2 × 5 min washes in 100% ethanol, 5 min washes in 90% ethanol/H_2O, 5 min washes in 80% ethanol/H_2O and a 5 min wash in 70% ethanol/H_2O and then incubated in 70% ethanol/H_2O with fluorescent probes (5 μM in DMSO) for 10 min. The location of plaques was confirmed by staining with 8C (5 μM in EtOH). Finally, the sections were washed with 30% ethanol and PBS (10 mM, pH = 7.4) and packed between a slide and cover glass. Fluorescence observation was performed using a confocal laser-scanning microscope (Zeiss LSM710, Germany). The excitation wavelength used for DM-BZ, PD-BZ, PD-NA and PD-NA-TEG was 405 nm and the corresponding collected wavelength is 525 ± 25 nm. As for 8C, the excitation

wavelength was 561 nm and the corresponding collected wavelength was 705 ± 45 nm.

Super-resolution imaging

The microscope is based on a commercial microscope stand (Olympus IX73P2F) and imaging was carried out using a 100 × 1.49 NA oil-immersion TIRF objective (UAPON 100XOTIRF, Olympus). Two solid-state lasers including a 405 nm solid-state laser (OBIS 405 LX, Coherent, 50 mW) and a 561 nm solid-state laser (OBIS 561 LS, Coherent, 150 mW) were used. A dichroic mirror (DM: ZT561rdc-xr, Chroma) and a single band filter (EM: ET630/75 m, Chroma) were used to separate the collected fluorescence from the scattering laser and impurity fluorescence. The HEWL fibril sample was dispersed on a clean coverslip by a simple drop-coating method. The coverslips with HEWL fibrils were then exposed to the atmosphere until the water evaporated completely under ambient conditions. For the super-resolution imaging experiments, a 50 μL solution of PD-NA-TEG (5 μM) in water containing 30 v/v% EtOH was dropped on the above as-prepared sample. Keeping the 405 nm laser on all the time, usually 5000 frames were recorded with an acquisition frequency of 50 Hz to get a good super-resolution image. The size of an individual pixel of the pictures in conventional optical imaging is 100 nm, while that is 10 nm for the reconstructed ones. The excitation wavelength of DM-BZ, PD-BZ, PD-NA and PD-NA-TEG was 405 nm and the collected wavelength was 525 ± 50 nm. The prepared sample was placed on a stage for super-resolution imaging with 405 nm laser exposure (15.3 W cm^{-2}) and the frame acquisition frequency was set to be 50 Hz. An ImageJ plugin written in Java was used to analyze the image. An ultra-fast and high-precision image analysis method, termed MaLiang (maximum likelihood algorithm encoded on a Graphics Processing Unit (GPU)), was employed to reconstruct the super-resolution images.[42]

Synthetic procedures

Synthesis of (6-bromonaphthalen-2-yl)methanol (compound 1). To a stirred mixture of 6-bromonaphthalene-2-carboxylic acid (20 g, 80 mmol, 1.00 eq.) in THF (60 mL) at 0 °C was added dropwise BH_3 (1 N in THF, 160 mL, 160 mmol, 2.00 eq.) under a N_2 atmosphere. The resulting mixture was stirred at ambient temperature for 16 h and then quenched with ice-water and extracted with EtOAc 3 times. The combined organic layers were washed with brine, dried over Na_2SO_4 and concentrated under vacuum to afford (6-bromonaphthalen-2-yl)methanol (18.1 g, crude) as a white solid, which was used for the next step without further purification. ^{1}H NMR (400 MHz, DMSO-d_6) δ (ppm): 8.17 (d, J = 2.4 Hz, 1H), 7.87 (d, J = 11.6 Hz, 2H), 7.61 (dd, J = 11.6, 2.8 Hz, 1H), 7.52 (dd, J = 11.2, 2.4 Hz, 1H), 4.66 (s, 2H).

Synthesis of 6-bromonaphthalene-2-carbaldehyde (compound 2). To a stirred solution of (6-bromonaphthalen-2-yl)methanol (18.1 g, 76.7 mmol, 1.00 eq.) in DCM (300 mL) at 0 °C was added PCC (34.6 g, 92.0 mmol, 1.20 eq.). The resulting mixture was stirred at ambient temperature for 16 h and then filtered. The filtrate was concentrated under vacuum. The residue was purified by flash chromatography on silica gel (10–70% DCM in petroleum ether) to afford 6-bromonaphthalene-2-carbaldehyde (12.8 g, 68% for two steps) as a white solid. ^{1}H NMR (400 MHz, DMSO-d_6) δ (ppm): 10.15 (s, 1H), 8.60 (s, 1H), 8.34 (s, 1H), 8.12 (d, J = 8.8 Hz, 1H), 8.05 (d, J = 8.4 Hz, 1H), 7.94 (d, J = 9.2 Hz, 1H), 7.78 (d, J = 9.6 Hz, 1H); MS (ESI, m/z): 235, 237 $(M + H)^+$.

Synthesis of 2-(6-bromonaphthalen-2-yl)-1,3-dioxolane (compound 3). A mixture of 6-bromonaphthalene-2-carbaldehyde (12.8 g, 54.7 mmol, 1.00 eq.), ethane-1,2-diol (50 mL, excess) and 4-methylbenzene-1-sulfonic acid (470 mg, 2.74 mmol, 0.05 eq.) in toluene (200 mL) was refluxed for 48 h with Dean Stark apparatus attached. The resulting mixture was washed with $NaHCO_3$ solution and brine, dried over Na_2SO_4 and concentrated under vacuum. The residue was purified by flash chromatography on silica gel (10–70% DCM in petroleum ether) to afford 2-(6-bromonaphthalen-2-yl)-1,3-dioxolane (7.3 g, 48%) as a light yellow solid. ^{1}H NMR (400 MHz, DMSO-d_6) δ (ppm): 8.23 (d, J = 2.4 Hz, 1H), 8.01 (s, 1H), 7.95 (d, J = 3.6 Hz, 1H), 7.92 (d, J = 3.2 Hz, 1H), 7.66 (dd, J = 11.6, 2.8 Hz, 1H), 7.60 (dd, J = 11.6, 2.0 Hz, 1H), 5.88 (s, 1H), 4.18–3.91 (m, 4H); MS (ESI, m/z): 279, 281 $(M + H)^+$.

Synthesis of 1-[6-(1,3-dioxolan-2-yl)naphthalen-2-yl]piperidine (compound 4). A mixture of 2-(6-bromonaphthalen-2-yl)-1,3-dioxolane (7 g, 25.18 mmol, 1.00 eq.), piperidine (4.28 g, 50.36 mmol, 2 eq.), Cs_2CO_3 (12.31 g, 37.77 mmol, 1.5 eq.), $(t\text{Bu})_3$P (10% in toluene, 18.8 g, 9.317 mmol, 0.37 eq.) and $Pd(OAc)_2$ (564 mg, 2.518 mmol, 0.1 eq.) in toluene (105 mL) was stirred at 110 °C for 16 h under a N_2 atmosphere and then filtered. The filtrate was concentrated under vacuum. The residue was purified by flash chromatography on silica gel (0–30% EtOAc in petroleum ether) to afford 1-[6-(1,3-dioxolan-2-yl)naphthalen-2-yl]piperidine (6.5 g, 91%) as a yellow solid. ^{1}H NMR (400 MHz, $CDCl_3$) δ (ppm): 7.82 (s, 1H), 7.73 (t, J = 9.2 Hz, 2H), 7.51 (dd, J = 8.8, 1.6 Hz, 1H), 7.31 (d, J = 8.8 Hz, 1H), 7.14 (s, 1H), 5.96 (s, 1H), 4.31–4.00 (m, 4H), 3.30 (t, J = 5.6 Hz, 4H), 1.85–1.73 (m, 4H), 1.65 (q, J = 5.9 Hz, 2H); MS (ESI, m/z): 284, 286 $(M + H)^+$.

Synthesis of 6-(piperidin-1-yl)naphthalene-2-carbaldehyde (compound 5). To a stirred mixture of 1-[6-(1,3-dioxolan-2-yl)naphthalen-2-yl]piperidine (6.5 g, 22.97 mmol, 1.00 eq.) in DCM (100 mL) at 0 °C was added dropwise TFA (26 mL). The resulting solution was stirred at ambient temperature for 16 h and then concentrated under vacuum. The residue was re-dissolved in THF. The resulting solution was washed with NaOH (1 N) and brine, dried over Na_2SO_4 and concentrated under vacuum. The residue was purified by trituration with DCM/hexane (1 : 5) to afford 6-(piperidin-1-yl)naphthalene-2-carbaldehyde (4.1 g, 75%) as a yellow solid. ^{1}H NMR (400 MHz, DMSO-d_6) δ (ppm): 10.00 (s, 1H), 8.33 (d, J = 2.0 Hz, 1H), 7.93 (d, J = 12.0 Hz, 1H), 7.82–7.65 (m, 2H), 7.47 (dd, J = 12.4, 3.6 Hz, 1H), 7.23 (d, J = 3.6 Hz, 1H), 3.41–3.38 (m, 4H), 1.73–1.55 (m, 6H); MS (ESI, m/z): 240 $(M + H)^+$.

Synthesis of DM-BZ, PD-BZ and PD-NA. A mixture of aldehyde (1 eq.), 2-(4-bromophenyl)acetonitrile (1.05 eq.) and t-BuOK (1 eq.) in EtOH was stirred at room temperature for 1 h. The solid was collected by filtration, washed with EtOH and dried in an oven at 50 °C to afford the target compounds as a yellow solid.

DM-BZ. ^{1}H NMR (600 MHz, $CDCl_3$) δ (ppm): 7.86 (d, J = 8.4 Hz, 2H), 7.54–7.49 (m, 4H), 7.39 (s, 1H), 6.76 (d, J = 8.4 Hz, 2H), 3.07 (s, 6H). ^{13}C NMR (151 MHz, $CDCl_3$) δ (ppm) 151.78, 142.80, 134.61, 131.97, 131.42, 126.91, 121.85, 121.37, 119.09, 111.66, 103.26, 40.08. MS (ESI, m/z): 327, 329 $(M + H)^+$, 368, 370 $(M + H + CH_3CN)^+$.

PD-BZ. ^{1}H NMR (600 MHz, $CDCl_3$) δ (ppm): 7.84–7.82 (m, 2H), 7.53–7.48 (m, 4H), 7.37 (s, 1H), 6.90 (d, J = 8.4 Hz, 2H), 3.35 (t, J = 5.2 Hz, 4H), 1.71–1.64 (m, 6H). ^{13}C NMR (151 MHz, $CDCl_3$) δ (ppm) 152.81, 142.51, 134.43, 132.00, 131.34, 126.98, 122.68, 122.07, 118.85, 114.26, 104.18, 48.69, 25.35, 24.31. MS (ESI, m/z): 367, 369 $(M + H)^+$.

PD-NA. ^{1}H NMR (600 MHz, $CDCl_3$) δ (ppm): 8.15 (s, 1H), 8.02 (dd, J = 9.0, 1.8 Hz, 1H), 7.75 (d, J = 9.0 Hz, 1H), 7.69 (d, J = 9.0 Hz, 1H), 7.59–7.55 (m, 5H), 7.31 (d, J = 9.0 Hz, 1H), 7.09 (s, 1H), 3.35 (t, J = 5.4 Hz, 4H), 1.76 (brs, 4H), 1.68–1.66 (m, 2H).^{13}C NMR (151 MHz, $CDCl_3$) δ (ppm) 151.26, 143.04, 136.12, 134.08, 132.11, 130.74, 129.73, 127.85, 127.27, 127.20, 125.61, 122.76, 119.86, 118.35, 109.10, 107.60, 49.97, 25.64, 24.35. MS (ESI, m/z): 417, 419 $(M + H)^+$.

Synthesis of PD-NA-TEG. A mixture of PD-NA (200 mg, 0.48 mmol, 1.00 eq.), 2-(4-(2-methoxyethoxy)phenyl)-4,4,5,5-tetramethyl-1,3,2-dioxaborolane (184 mg, 0.50 mmol, 1.05 eq.), K_2CO_3 (166 mg, 0.60 mmol, 2.5 eq.) and $Pd(PPh_3)_4$ (56 mg, 0.048 mmol, 0.1 eq.) in toluene/water (10 mL/3 mL) was stirred at 90 °C for 16 h under a N_2 atmosphere. To this was added EtOAc (50 mL) and the resulting mixture was washed with water and brine, dried over Na_2SO_4 and concentrated under vacuum. The residue was purified by flash chromatography on silica gel (20–70% DCM in petroleum ether) to afford PD-NA-TEG (53 mg, 18%) as a yellow solid. ^{1}H NMR (600 MHz, $CDCl_3$) δ (ppm): 8.16 (s, 1H), 8.04 (dd, J = 8.4, 1.8 Hz, 1H), 7.77–7.73 (m, 3H), 7.70 (d, J = 8.4 Hz, 1H), 7.64–7.62 (m, 3H), 7.57–7.54 (m, 2H), 7.30 (d, J = 9.0 Hz, 1H), 7.09 (s, 1H), 7.02–7.00 (m, 2H), 4.18 (t, J = 4.8 Hz, 2H), 3.89 (t, J = 4.8 Hz, 2H), 3.77–3.75 (m, 2H), 3.71–3.66 (m, 4H), 3.57–3.55 (m, 2H), 3.39 (s, 3H), 3.34 (t, J = 6.0 Hz, 4H), 1.77–1.74 (m, 4H), 1.70–1.63 (m, 2H).^{13}C NMR (151 MHz, $CDCl_3$) δ (ppm): 158.74, 142.04, 141.07, 135.93, 133.34, 132.69, 130.42, 129.67, 128.28, 128.00, 127.26, 127.15, 127.07, 126.16, 125.75, 119.89, 118.71, 115.05, 109.22, 108.55, 71.95, 70.87, 70.68, 70.60, 69.74, 67.54, 59.05, 50.07, 25.67, 24.36. MS (ESI, m/z): 289 $(M/2 + H)^+$, 577 $(M + H)^+$.

Conflicts of interest

There are no conflicts to declare.

Acknowledgements

This work was supported by the 973 Program of China (2015CB755602 and 2013CB922104), NSFC (21474034, 51673077 and 51603078), the Fundamental Research Funds for the Central Universities (HUST: 2016YXMS029), and the Natural Science Foundation of Hubei Province (2018CFB574). We also thank the Analytical and Testing Center of Huazhong University of Science and Technology, the Center for Nanoscale Characterization & Devices (CNCD) and the Center of Micro-Fabrication and Characterization (CMFC), WNLO of HUST for use of their facilities.

Notes and references

1 L. Minati, T. Edginton, M. G. Bruzzone and G. Giaccone, *Am. J. Alzheimer's Dis. Other Demen.*, 2009, **24**, 95–121.
2 I. W. Hamley, *Chem. Rev.*, 2012, **112**, 5147–5192.
3 J.-Y. Zhu, L.-F. Zhou, Y.-K. Li, S.-B. Chen, J.-W. Yan and L. Zhang, *Anal. Chim. Acta*, 2017, **961**, 112–118.
4 H. Fu, M. Cui, L. Zhao, P. Tu, K. Zhou, J. Dai and B. Liu, *J. Med. Chem.*, 2015, **58**, 6972–6983.
5 H. Fu, P. Tu, L. Zhao, J. Dai, B. Liu and M. Cui, *Anal. Chem.*, 2016, **88**, 1944–1950.
6 J. Mei, N. L. Leung, R. T. Kwok, J. W. Lam and B. Z. Tang, *Chem. Rev.*, 2015, **115**, 11718–11940.
7 Q. Yang, Z. Ma, H. Wang, B. Zhou, S. Zhu, Y. Zhong, J. Wang, H. Wan, A. Antaris, R. Ma, X. Zhang, J. Yang, X. Zhang, H. Sun, W. Liu, Y. Liang and H. Dai, *Adv. Mater.*, 2017, **29**, 1605497.
8 Z. Q. Guo, S. Park, J. Yoon and I. Shin, *Chem. Soc. Rev.*, 2014, **43**, 16–29.
9 A. Cerussi, N. Shah, D. Hsiang, A. Durkin, J. Butler and B. J. Tromberg, *J. Biomed. Opt.*, 2006, **11**, 16.
10 M. Heilemann, S. van de Linde, A. Mukherjee and M. Sauer, *Angew. Chem., Int. Ed.*, 2009, **48**, 6903–6908.
11 M. Fernandez-Suarez and A. Y. Ting, *Nat. Rev. Mol. Cell Biol.*, 2008, **9**, 929–943.
12 G. T. Dempsey, J. C. Vaughan, K. H. Chen, M. Bates and X. Zhuang, *Nat. Methods*, 2011, **8**, 1027–1036.
13 J. Yan, L.-X. Zhao, C. Li, Z. Hu, G.-F. Zhang, Z.-Q. Chen, T. Chen, Z.-L. Huang, J. Zhu and M.-Q. Zhu, *J. Am. Chem. Soc.*, 2015, **137**, 2436–2439.
14 W.-L. Gong, J. Yan, L.-X. Zhao, C. Li, Z.-L. Huang, B. Z. Tang and M.-Q. Zhu, *Photochem. Photobiol. Sci.*, 2016, **15**, 1433–1441.
15 J.-X. Liu, B. Xin, C. Li, N.-H. Xie, W.-L. Gong, Z.-L. Huang and M.-Q. Zhu, *ACS Appl. Mater. Interfaces*, 2017, **9**, 10338–10343.
16 R. Hu, N. L. Leung and B. Z. Tang, *Chem. Soc. Rev.*, 2014, **43**, 4494–4562.
17 X. Gao, G. Feng, P. N. Manghnani, F. Hu, N. Jiang, J. Liu, B. Liu, J. Z. Sun and B. Z. Tang, *Chem. Commun.*, 2017, **53**, 1653–1656.
18 J. Zhang, Z. Liu, P. Lian, J. Qian, X. Li, L. Wang, W. Fu, L. Chen, X. Wei and C. Li, *Chem. Sci.*, 2016, **7**, 5995–6005.
19 Y. Sun, C. Qu, H. Chen, M. He, C. Tang, K. Shou, S. Hong, M. Yang, Y. Jiang, B. Ding, Y. Xiao, L. Xing, X. Hong and Z. Cheng, *Chem. Sci.*, 2016, **7**, 6203–6207.
20 Y.-F. Wang, T. Zhang and X. Liang, *Small*, 2016, **12**, 6451–6477.
21 X. Wang, J. Hu, G. Zhang and S. Liu, *J. Am. Chem. Soc.*, 2014, **136**, 9890–9893.
22 C. Li, T. Wu, C. Hong, G. Zhang and S. Liu, *Angew. Chem., Int. Ed.*, 2012, **51**, 455–459.

23 Q.-Y. Zhou, C. Fan, C. Li, Y.-L. Wang, Z.-Q. Chen, Q. Yu and M.-Q. Zhu, *Mater. Horiz.*, 2018, **5**, 474–479.
24 M. Cui, M. Ono, H. Watanabe, H. Kimura, B. Liu and H. Saji, *J. Am. Chem. Soc.*, 2014, **136**, 3388–3394.
25 W. M. Chang, M. Dakanali, C. C. Capule, C. J. Sigurdson, J. Yang and E. A. Theodorakis, *ACS Chem. Neurosci.*, 2011, **2**, 249–255.
26 M. Ono, H. Watanabe, H. Kimura and H. Saji, *ACS Chem. Neurosci.*, 2012, **3**, 319–324.
27 P. L. Donabedian, T. K. Pham, D. G. Whitten and E. Y. Chi, *ACS Chem. Neurosci.*, 2015, **6**, 1526–1535.
28 Y. Hong, L. Meng, S. Chen, C. W. T. Leung, L.-T. Da, M. Faisal, D.-A. Silva, J. Liu, J. W. Y. Lam, X. Huang and B. Z. Tang, *J. Am. Chem. Soc.*, 2012, **134**, 1680–1689.
29 H. Shi, J. Liu, J. Geng, B. Z. Tang and B. Liu, *J. Am. Chem. Soc.*, 2012, **134**, 9569–9572.
30 N. Pradhan, D. Jana, B. K. Ghorai and N. R. Jana, *ACS Appl. Mater. Interfaces*, 2015, **7**, 25813–25820.
31 S. G. S. Kaminski, S. van de Linde, M. Erdelyi, E. K. Esbjorner, T. Klein, E. Rees, C. W. Bertoncini, C. M. Dobson, M. Sauer and C. F. Kaminski, *J. Am. Chem. Soc.*, 2011, **133**, 12902–12905.
32 W. C. Duim, Y. Jiang, K. Shen, J. Frydman and W. E. Moerner, *ACS Chem. Biol.*, 2014, **9**, 2767–2778.
33 J. Ries, V. Udayar, A. Soragni, S. Hornemann, K. P. Nilsson, R. Riek, C. Hock, H. Ewers, A. A. Aguzzi and L. Rajendran, *ACS Chem. Neurosci.*, 2013, **4**, 1057–1061.
34 D. Pinotsi, A. K. Buell, C. Galvagnion, C. M. Dobson, G. S. Schierle and C. F. Kaminski, *Nano Lett.*, 2014, **14**, 339–345.
35 H. A. Shaban, C. A. Valades-Cruz, J. Savatier and S. Brasselet, *Sci. Rep.*, 2017, **7**, 12482.
36 X. Y. Shen, Y. J. Wang, E. Zhao, W. Z. Yuan, Y. Liu, P. Lu, A. Qin, Y. Ma, J. Z. Sun and B. Z. Tang, *J. Phys. Chem. C*, 2013, **117**, 7334–7347.
37 H. Tong, Y. Hong, Y. Dong, Y. Ren, M. Häussler, J. W. Y. Lam, K. S. Wong and B. Z. Tang, *J. Phys. Chem. B*, 2007, **111**, 2000–2007.
38 A. Shao, Y. Xie, S. Zhu, Z. Guo, S. Zhu, J. Guo, P. Shi, T. D. James, H. Tian and W.-H. Zhu, *Angew. Chem., Int. Ed.*, 2015, **54**, 7275–7280.
39 C. Wu, Z. Wu, B. Wang, X. Li, N. Zhao, J. Hu, D. Ma and Q. Wang, *ACS Appl. Mater. Interfaces*, 2017, **9**, 32946–32956.
40 W. Liu, S. Ying, Q. Zhang, S. Ye, R. Guo, D. Ma and L. Wang, *Dyes Pigm.*, 2018, **158**, 204–212.
41 G.-F. Zhang, M. P. Aldred, W.-L. Gong, C. Li and M.-Q. Zhu, *Chem. Commun.*, 2012, **48**, 7711–7713.
42 T. Quan, P. Li, F. Long, S. Zeng, Q. Luo, P. N. Hedde, G. U. Nienhaus and Z.-L. Huang, *Opt. Express*, 2010, **18**, 11867–11876.

